Electrolytic transport through a synthetic nanometer-diameter pore

Chuen Ho*, Rui Qiao†, Jiunn B. Heng*, Aveek Chatterjee†, Rolf J. Timp‡, Narayana R. Aluru†, and Gregory Timp*§

*Department of Electrical and Computer Engineering and †Department of Mechanical and Industrial Engineering, University of Illinois, Urbana, IL 61801; and ‡Stanford University, Stanford, CA 94305

We have produced single, synthetic nanometer-diameter pores by using a tightly focused, high-energy electron beam to sputter atoms in 10-nm-thick silicon nitride membranes. Subsequently, we measured the ionic conductance as a function of time, bath concentration, and pore diameter to infer the conductivity and ionic mobility through the pores. The pore conductivity is found to be much larger than the bulk conductivity for dilute bath concentrations, where the Debye length is larger than the pore radius, whereas it is comparable with or less than the bulk for high bath concentrations. We interpret these observations by using multiscale simulations of the ion transport through the pores. Molecular dynamics is used to estimate the ion mobility, and ion transport in the pore is described by the coupled Poisson–Nernst–Planck and the Stokes equations that are solved self-consistently for the ion concentration and velocity and electrical potential. We find that the measurements are consistent with the presence of fixed negative charge in the pore wall and a reduction of the ion mobility because of the fixed charge and the ion proximity to the pore wall.

ion conduction | nanopore | nanostructured materials

Nanometer-diameter pores formed by proteins are prevalent in biology where they are used to regulate the flow of ions and molecules through the otherwise impermeable cell membrane. Even though the structure is known with atomic precision in some cases, there does not seem to be a simple relationship between the pore geometry and the conductivity (1). This difficulty may be due to the nonuniform, high concentration of charge in the pore (2).

As a first step toward understanding the conductivity, we produced synthetic pores ranging in diameter from 1 to 3.2 nm in ultra-thin silicon nitride (Si_3N_4) membranes and measured the ionic conductance as a function of time and electrolyte concentration to infer the conductivity and ionic mobility. This work measures the conductance through pores with radii comparable with the van der Waals radius of an ion (3–5). Similar claims by Siwy and Fuliński (6) that rely on the conductance through a single pore to estimate the pore diameter are unreliable, because conductance does not scale with the diameter. Like previous work in nanofiltration membranes that contain ensembles of pores with varying diameter (7), we find that the pore conductivity associated with a single pore is found to be much larger than the bulk conductivity for dilute electrolyte concentrations, where the Debye length is larger than the pore radius, whereas it is comparable with or less than the bulk for high concentrations. These observations are also consistent with a recent report by Stein *et al.* (8) of ion transport in silica channels >70 nm wide that is governed by surface charge. To interpret our observations, we use multiscale simulations of the ion transport through the pores. Molecular dynamics (MD) is used to estimate the ion mobility, and ion transport in the pore is described by the coupled Poisson–Nernst–Planck (PNP) (9) and Stokes (10) equations, which are solved self-consistently for the ion concentration and velocity and electrical potential (11). We find that the measurements are consistent with an inhomogeneous electrolyte distribution within the pore, corresponding to the presence of fixed negative charge at the pore wall and a reduction of the ion mobility because of the fixed charge and the ion proximity to the pore wall.

Materials and Methods

We formed Si, SiO_2, and Si_3N_4 membranes by using conventional semiconductor microfabrication practices. We found that membranes fabricated this way are robust, withstanding hundreds of electrolyte immersion and emersion cycles without failing. Subsequently, a single nanopore is created in the membrane by electron beam stimulated decomposition and sputtering by using a JEOL 2010F transmission electron microscope (TEM) operating at 200 keV (1 eV = 1.602×10^{-19} J), which is able to generate a tightly focused beam as small as 0.5 nm (Gaussian width) in diameter. This lithography strategy to produce synthetic pores in ultra-thin membranes is superior to schemes that use focused ion beam milling (12) or ion-tracks in conjunction with a deposition (13) because of the high resolution and flux available with an electron beam, and, unlike regrowth schemes, it is applicable to a wide variety of membrane materials (14, 15). Generally, pores fabricated this way do not have a uniform diameter throughout the thickness of the membrane, however.

Fig. 1*a* is a TEM image taken at a tilt angle of 0° of a pore with apparent radius of 0.9 ± 0.1 nm in a Si_3N_4 membrane nominally 10-nm thick. The thickness of similarly processed Si_3N_4 membranes was determined to be 10 ± 2 nm by using scanning electron microscopy and 11 ± 3 nm by using electron energy loss spectroscopy. The TEM image in Fig. 1*a* represents a 2D projection through the membrane. The shot noise observed in the central area identified with the pore indicates perfect transmission of electrons through the membrane in that area. To investigate the 3D structure, we tilted the membrane in the TEM about the pore axis and explored various defocus conditions, as illustrated by Fig. 1*b*. Fig. 1*b* can be interpreted as a projection through a pore that is partially occluded by the walls of the membrane in the direction perpendicular to the 15° tilt. By using images like this one, we have developed models for the pore geometry, one of which is represented by two intersecting cones with a 10° cone angle, as illustrated in Fig. 1*c*. This interpretation of the TEM images is not unique, however. A single cone with the same angle also could be used to describe these data, as well. The ambiguities in pore geometry along with the TEM resolution give rise to uncertainty in the conductivity.

To determine the conductivity, we measured the dc electrolytic current through a single pore as a function of the applied electrochemical potential at 23.5 ± 1°C in a membrane transport bi-cell made of acrylic, where the membrane separates two identical compartments, each containing ≈1 ml of electrolyte and a Ag/AgCl electrode positioned ≈1 mm from the mem-
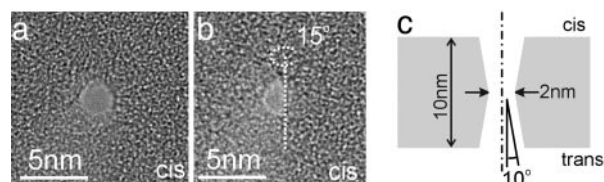
ENGINEERING

Fig. 1. TEM characterization of a synthetic nanopore. Nanopores are produced by using a tightly focused, high-energy electron beam. (*a*) A TEM image of a nanopore (slightly out of focus to exaggerate the pore) in a 10-nm-thick Si₃N₄ membrane viewed at 0° tilt angle. The apparent radius of the pore is ≈0.9 ± 0.1 nm. (*b*) A TEM image of the same pore shown in *a* but viewed at a 15° tilt angle. By using projections like this one, we can infer the 3D structure of the pore. (*c*) A (nonunique) schematic representation of the nanopore consistent with the images shown in *a* and *b*, consisting of two intersecting cones with a 10° cone angle.

brane. In a typical measurement, which takes <15 min, a constant voltage bias is applied between the electrodes until a steady-state current is established and measured by using an Axopatch 200B amplifier with a 10-kHz bandwidth. The measured current was found to be independent of the relative electrode-membrane distance from 1 to 10 mm for all concentrations of electrolyte used in these experiments. Most of our experiments were executed by using calibrated KCl solutions (LabChem, Inc., Pittsburgh) because the potassium (K^+) and chloride (Cl^-) ions are monovalent and are known to have approximately the same mobility in bulk ($\mu_K^{bulk} \approx \mu_{Cl}^{bulk} = 7.7 \times 10^{-8}$ m²·V⁻¹·s⁻¹ at infinite dilution). To investigate the effect on the cation mobility, we sparingly used NaCl solutions ($\mu_{Na}^{bulk} \approx 4.6 \times 10^{-8}$ m²·V⁻¹·s⁻¹ at infinite dilution) as well.

Results

Fig. 2 *a–c* shows the current–voltage (*I–V*) characteristics obtained from pores with apparent radii of 0.5 ± 0.1, 1.0 ± 0.1, and 1.5 ± 0.1 nm, respectively, measured over a range of ±1 V in 1 M KCl after >55 h of immersion in deionized water. Notice that in all cases, the *I–V* characteristics are approximately linear, in contrast with work on asymmetrical conical pores in polymer membranes (8). A line fit to the data (red dashed lines) yields the conductance 0.63 ± 0.03, 1.09 ± 0.03, and 1.24 ± 0.03 nS, respectively, which can only be attributed to the pore because the measured series resistance due to the electrolyte reservoirs, probes, and wiring contribute only <5 kΩ. However, it is apparent that the conductance does not scale linearly with the radius derived from TEM. In Fig. 2*d*, we have juxtaposed the conductance, $G = \partial I / \partial V |_{V=100mV}$, measured through a number of pores characterized by an effective pore radius, R_p, alongside the conductance of a membrane without a pore. To account for

elliptical shape, R_p is taken to be the geometric mean of the major and minor axis of the pore.

The electrolytic conductance through the pore is measured at regular short intervals (<15 min). After each measurement, the electrolyte is flushed and subsequently replaced by deionized water. When another measurement is to be performed, the electrolyte is replenished from a calibrated solution. The pore conductance generally increases dramatically with time during the first 20 h and eventually saturates, whereas the membrane conductance is <3.5 pS and time-independent. The time-dependence of the conductance through single nanopores measured this way is reproducible (within ≈10%) after a pore is dried for an extended period and then reexamined following the same procedures. (For economy, we have focused here exclusively on measurements in Si₃N₄ membranes. A similar time-dependence for the conductance is observed in pores fabricated by using the same methodology outlined above in membranes in Si and SiO₂.)

As Fig. 2*d* indicates, ions only reluctantly permeate the membrane through the nanopore before the first 20 h. We tentatively attribute this observation to the dynamics associated with wetting the pore. It has been shown that electrical conductance measurements can be used to evaluate capillary-wetting rates (16). When an electrolytic solution is used as a wetting liquid, the ionic current between the electrodes increases as the liquid wets the capillary (or pore). After the wetting transition is complete, the conductance remains constant, independent of time, at a value that corresponds to the electrical conductance of the wetting liquid. Accordingly, the low conductance (<3 pS) found initially through all of the pores could be interpreted as a metastable vapor phase (a nanometer-scale bubble) initially plugging the pore and precluding any electrolytic current (17–20).

The measured electrolytic conductance through single pores in separate membranes measured after the conductance saturates ($t > 55$ h) in 1 M, 100 mM, and 10 mM KCl electrolyte is shown in Fig. 3 *a*, *c*, and *e*, respectively, plotted as a function of $1/R_p$. In each case, the conductance is linear with the applied voltage over the range of ±200 mV. The corresponding conductivity, calculated by assuming the two-cone geometry, a uniform ion mobility, and concentration throughout the pore volume, is shown in Fig. 3 *b*, *d*, and *f*, respectively. The error in conductivity is predominantly due to the uncertainty in pore geometry and variations in the conductance with time. We find that the conductivity fluctuates from pore to pore but is generally less than the bulk value for 1 M KCl solution ($\sigma_{bulk} \approx 10 S/m$, which is represented by the open circle at $1/R_p \rightarrow 0$).

In principle, three mechanisms contribute to electrolyte transport through the pore: electrophoretic ion migration, convection (i.e., electro-osmosis), and diffusion. However, as described below, we have calculated the contribution of the electrical migration, convection, and diffusion to the total ionic conduc-
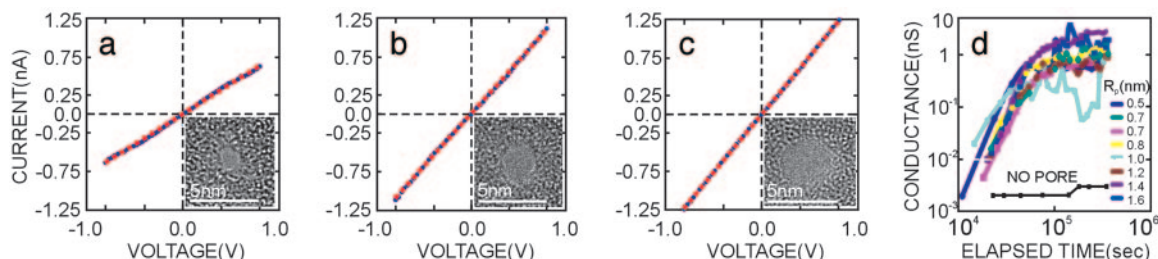

Fig. 2. The current–voltage (*I–V*) characteristics of a nanopore are approximately linear. (*a–c*) Measurements in 1 M KCl solution of the *I–V* characteristics of three pores with apparent radii of 0.5 ± 0.1, 1.0 ± 0.1, and 1.5 ± 0.1 nm, respectively. (*Insets*) The TEM image of the pore at 0° tilt. The pores are in separate Si₃N₄ membranes that are ≈10 nm thick. The (red) dashed lines represent least-squares fit to the data yielding slopes of 0.63 ± 0.03, 0.74 ± 0.03, and 1.24 ± 0.03 nS, respectively. (*d*) The time-dependence of similar measurements of conductance through various nanopores in the same type of membrane, where R_p ranges from 0.5 to 1.6 nm, all measured in 1 M KCl solution. Superimposed on this plot is the conductance through a membrane without a pore.
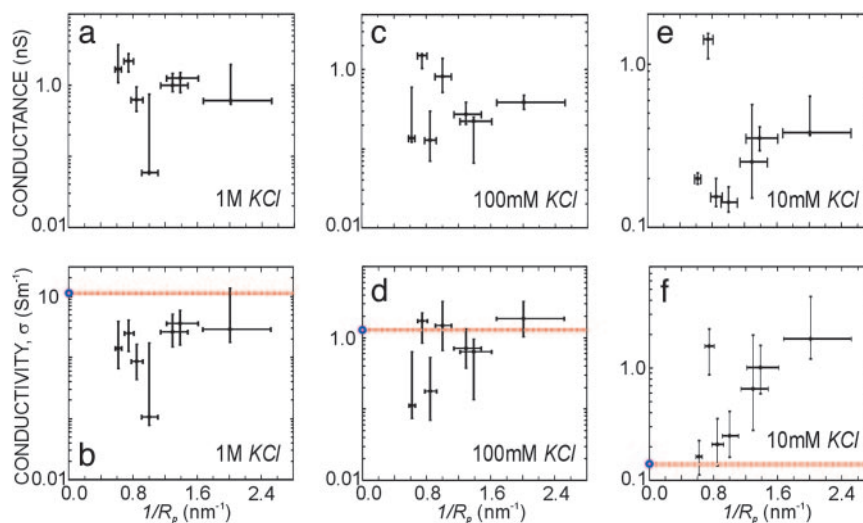
Fig. 3. The conductance (*a*, *c*, and *e*) and conductivity (*b*, *d*, and *f*) vs. the reciprocal of R_p. The conductance was measured at $t > 55$ h for the same seven pores at three different KCl concentrations, 1, 0.1, and 0.01 M. The open data points represent the bulk conductivity supplied by the vendor for the calibrated electrolytes used in the measurements.

tivity and found that for all of the pores studied, the contribution from ion migration predominates; it represents 95% of the total conductivity. The contributions of convection and diffusion are marginal. Following Schmid and Schwarz (7), the observed concentration dependence of the conductivity suggests that there is a fixed charge in the pore. Heuristically, if we ignore interionic forces that cause mobile counterions to accumulate in the vicinity of the fixed charge, assuming instead that counterions are distributed uniformly throughout the volume of the pore and that the corresponding mobility is uniform throughout the volume of the pore, then we can estimate the conductivity. If c is the bulk electrolytic concentration and c_p represents the concentration of (negative) charges at the pore wall, then charge neutrality ($c_K = c_{Cl} + c_p$) and the law of mass-action ($c_K c_{Cl} = c^2$) constrain the anion and cation concentration inside the pore. By using these relations, c_K and c_{Cl} can be calculated once c_p is determined. The ratio of the conductivity of the pore to the bulk follows from

$$\frac{\sigma_{\text{pore}}}{\sigma_{\text{bulk}}} = \frac{\mu_K^{\text{pore}} + \mu_{Cl}^{\text{pore}}}{\mu_K^{\text{bulk}} + \mu_{Cl}^{\text{bulk}}} \sqrt{1 + \left(\frac{c_p}{2c}\right)^2} + \frac{\mu_K^{\text{pore}} - \mu_{Cl}^{\text{pore}}}{\mu_K^{\text{bulk}} + \mu_{Cl}^{\text{bulk}}} \frac{c_p}{2c}.$$

[1]

According to this naïve analysis, the observed variations in the conductivity can be attributed to the differences in the fixed charge density and ionic mobility, especially for cations, in the pores. By fitting the conductivity data as a function of electrolytic concentration, it is possible to extract rudimentary estimates of the fixed charge density and the ion mobility in the pore. Table 1 summarizes the results of the least rms error fit of Eq. **1** to the conductivity data. Because of the presence of fixed negative charge in the pore, the conductivity is essentially determined by the concentration and mobility of the cation for 0.01 M $< c <$ 1 M, which gives rise to a disproportionate uncertainty in the anion mobility. To appreciate the wide latitude in the fits, the rms error derived from the optimum fit was doubled and used as a convergence criterion. The resulting values obtained for c_p, μ_K, μ_{Na}, and μ_{Cl}, are indicated in parentheses in Table 1. We find a negative charge density in the pore that is typically >100 mM. We interpret these data to be consistent with a negative charge density in the pore that is typically >100 mM. This interpretation is equivocal, however. Notice that for the $R_p = 0.72$ nm pore, the

cation mobility is reduced while the anion mobility is approximately constant when the electrolyte is changed from KCl to NaCl as expected from the bulk mobilities, but the inferred charge density in the same pore is not identical.

This interpretation of ion transport, which assumes a uniform ion concentration and mobility throughout the volume of the pore, is problematic, especially when the Debye length and the van der Waals radius of the ions become comparable with the pore radius. For an accurate assessment with atomic detail, we simulated the ion transport in cylindrical Si_3N_4 pores by using MD and then calculated the conductance by using coupled PNP (9) and the Stokes (10) equations. First, to determine the effect of using a cylindrical approximation for a conical nanopore on the conductivity, we performed separate numerical simulations by using the double-cone structure of the nanopore as indicated by the TEM images. These simulations indicate that for $R_p = 0.5$ nm, the conductivity for conical structure is ≈12% higher than that of a cylindrical pore with the same radius. For all other pores, the difference in conductivity for cylindrical and conical

Table 1. Fixed charges, c_p, and ionic mobilities, μ, in the pores, estimated by fitting the conductivity data of each pore as a function of concentration using Eq. 1

R_p, nm	c_p, M	μ_K, μ_{Na}, $\times 10^{-8}$ m²·V⁻¹·s⁻¹	μ_{Cl}, $\times 10^{-8}$ m²·V⁻¹·s⁻¹
0.50	0.6 (0.3)	3.5 (6.3)	4 ± 8 (1 ± 4)
0.72	2.4 (0.3)	0.5 (3.6)	6 ± 5 (−1 ± 2)
0.72*	21.7 (0.2)	0.04 (2.2)	7 ± 10 (−2 ± 1)
0.78	0.2 (0.2)	3.3 (3.4)	−1 ± 2 (−1 ± 2)
1.00†			
1.19	1.8 (0.2)	0.1 (1.0)	8 ± 5 (3 ± 3)
1.34	0.5 (0.4)	3.6 (4.8)	−3 ± 2 (−4 ± 2)
1.45	0.7 (0.4)	1.2 (2.0)	−1 ± 1 (1 ± 0.4)
1.62	0.2 (0.1)	1.1 (2.6)	0 ± 1 (−2 ± 1)

The optimal values of the pore parameters that correspond to the minimum rms error of Eq. **1** are represented by the numbers outside the parentheses; the numbers inside the parentheses correspond to a rms error that is two times larger than the minimum.
*The conductivity data for this pore is inferred from conductance measurements in NaCl solutions at 0.01, 0.1, and 0.85 M.
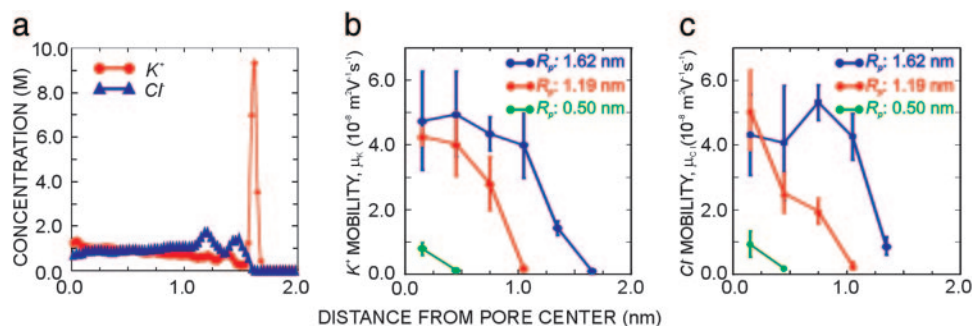†The conductivity data for this pore cannot be fit by Eq. **1**.

Ho *et al.*

Fig. 4. Variation of ion cencentration and mobility in pores of various diameter. (*a*) Ion concentration distribution in the 1.62-nm-radius Si_3N_4 pore from MD simulations. A significant amount of K^+ ions are adsorbed on the pore surface, and the ion distribution in the pore center is bulk-like. (*b* and *c*) K^+ (*b*) and Cl^- (*c*) ion mobility variation in three Si_3N_4 pores with R_p of 1.62, 1.19, and 0.50 nm. The ion mobility is affected by both the ion–surface interactions and the confinement, which is substantially lower near the pore surface compared with that in the pore center. Also, the ion mobility in the entire pore decreases dramatically as R_p decreases.

geometry is <3% because the cone angle is small (≈10°), and the ion transport through a double-cone structure pore depends primarily on the narrowest portion of the pore, Moreover, using a conical structure requires modeling the entire Si_3N_4 pore and a corresponding portion of the bath, which makes the MD simulations time-consuming without offering additional insights into the ion transport. In contrast, by using a cylindrical pore, periodic boundary conditions can be used along the axial direction to facilitate the MD computations. So, we adopt a cylindrical pore as a reasonable and economical approximation to be used instead of a double-cone structured pore in all of the subsequent calculations.

To construct the pore, a cubic unit cell of Si_3N_4 crystal (21) was first replicated in three dimensions to produce a cubic box of Si_3N_4 membrane. Two cubic boxes of the same thickness (4.64 nm) and different cross-sectional area (6.19 × 6.19 and 5.42 × 5.42 nm²) were used to accommodate pores of different diameters. The cylindrical nanopores were drilled by removing the atoms satisfying $\sqrt{(x-x_c)^2+(y-y_c)^2} < R_p + \delta$ (regardless of their z-coordinates), where (x, y) is the coordinate of the atom, (x_c, y_c) is the coordinate of the center of the pore, and δ is the van der Waals radii of the pore surface atoms (taken as 0.16 nm). The length of the pores equals the membrane thickness. The larger pores (R_p = 1.19 and 1.62 nm), where the ion concentration distribution in the pore center is bulk-like, were filled with KCl solution such that the concentrations of K^+/Cl^- ion and water in the pore center are 1.0 and 53.5 M, respectively. For the small pore (R_p = 0.5 nm), where the ion concentration in the pore center is not bulk-like, the Si_3N_4 membrane was immersed in 1.0 M KCl solution.

In the MD simulations, the Si and N atoms were modeled as Lennard–Jones atoms and were assigned partial charges reported in ref. 22. When the pores were constructed by the simulation procedure discussed above, the total charge of the Si_3N_4 membrane is typically nonzero. To maintain the electroneutrality, we adjusted the partial charge on the Si atom such that the total charge of the membrane is zero (23). The adjustment made to the charge was <0.2% of its absolute value. A Si_3N_4 surface immersed in an electrolyte solution usually carries a net surface charge. In this work, we assume a negative surface charge density of -0.02 C/m² on the pore surface, which is typical of a Si_3N_4 surface immersed in a solution of pH 7–8 (24, 25). To represent the net surface charge density, we added additional charges to the surface atoms of the Si_3N_4 pore. The additional charges are balanced by the excess amount of counterions in the simulation system. Water is modeled by using the SPC/E model (26), and ions are modeled as charged Lennard–Jones spheres. The Lennard–Jones parameters for water and

ions are taken from ref. 4, and those for the Si and N atoms are taken from the GROMACS force field (27).

MD simulations were performed by using a modified GROMACS package (27, 28). A cutoff radius of 1.1 nm was used to compute the Lennard–Jones potential. The electrostatic interactions were computed by using the Particle–Mesh–Ewald method (29) with no truncation for the Coulomb interactions. A cutoff distance of 1.10 nm was used in the calculation of electrostatic interactions in the real space. A fast Fourier transform grid spacing of 0.11 nm and cubic interpolation for charge distribution were chosen to compute the electrostatic interactions in the reciprocal space. The temperature of the fluid was maintained at 300 K by using a Berendsen thermostat. An electric field of 0.12 V/nm was applied in the z-direction. Starting from a random configuration, the systems were simulated for 1 ns to reach a steady state, followed by a production run of 6–10 ns. The ion distribution in the pore was computed by using the binning method, and the ion velocity was computed by tracking the positions of the ions (30).

Fig. 4*a* shows the ion concentration profile in a pore (R_p = 1.62 nm) obtained from MD simulations, indicating that a large amount of K^+ ions are adsorbed on the pore surface and the K^+ concentration oscillates as it approaches the center of the pore. Although the surface carries only a small net charge, the partial charges on the surface atoms can generate locally a strong electric field that attracts ions. The adsorption of K^+ ions at the pore surface overscreens the pore surface charge, hence the Cl^- ion concentration exceeds that of the K^+ ion for r < 1.55 nm. Notice that the Cl^- concentration also oscillates with distance from the pore wall. The oscillations in K^+/Cl^- concentrations are correlated with water density oscillations, which have been described in earlier reports (31, 32). Similar ion concentration distributions are observed in pores with smaller radii.

Fig. 4*b* shows the variation of K^+ ion mobility in the three Si_3N_4 pores with R_p of 1.62, 1.19, and 0.50 nm, respectively, obtained from MD simulations. Notice that the mobility of the absorbed K^+ ions is low ($\mu_K < 1 \times 10^{-8}$ m²·V^{-1}·s^{-1}) compared with the bulk value of K^+ mobility at 1 M KCl ($\mu_K^{bulk} \approx 5.5 \times 10^{-8}$ m²·V^{-1}·s^{-1}). However, the ion mobility gradually increases as it moves away from the surface toward the center of the pore. The large statistical error near the pore center is due to the small bin size. In the two larger pores, the mobilities near the center of the pore are almost the same and are comparable with the bulk value, whereas for the R_p = 0.50 nm pore, the K^+ ion mobility in the pore center is only ≈12% of its bulk value. Such a low mobility is due to confinement and is consistent with earlier reports (5, 33). Fig. 4*c* shows the variation of Cl^- ion mobility in the same pores. Similar trends for the K^+ and Cl^- ion mobilities are observed, indicating that the ion mobility in nanopores (R_p =
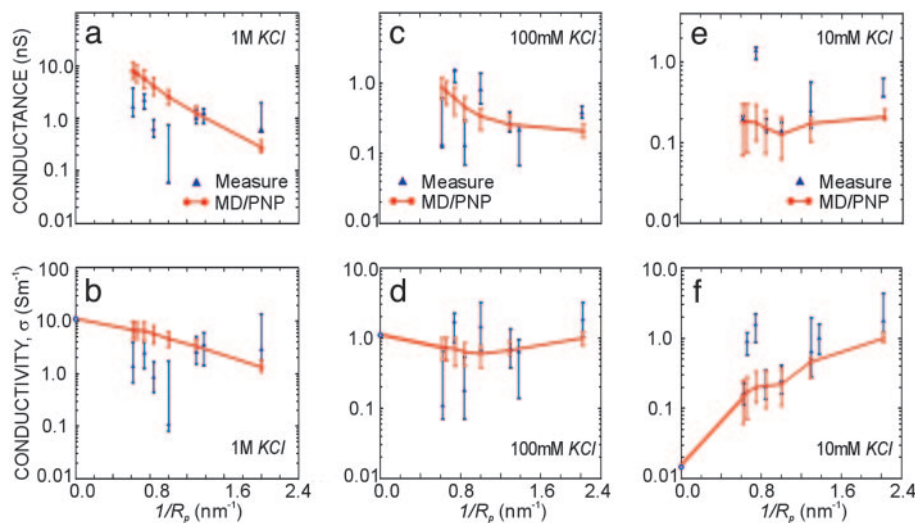
Fig. 5. Variation of conductance and conductivity with bath concentration in pores of various diameter. (*a* and *b*) Comparison of the conductance (*a*) and conductivity (*b*) as obtained from measurements and combined MD/PNP simulations, by using the bath concentration of 1.0 M KCl. The conductivity increases as the pore size increases and is always lower than bulk conductivity. (*c–f*) Comparison of the conductance (*c* and *e*) and conductivity (*d* and *f*) as obtained from experiments and combined MD/PNP simulations. Values were obtained by using a bath concentration of 100 mM (*c* and *d*) or 10 mM (*e* and *f*) KCl. The conductivity dependence on the pore size is weaker for 100 mM than for the 1.0 M case. Conversely, the conductivity increases as the pore size decreases for the 10 mM case.

0.5–1.6 nm) is substantially affected by confinement and ion–surface interactions.

Although MD simulations can be used to estimate the ionic conductance and conductivity of a nanopore immersed in electrolytic solutions at low bath concentrations, an excessively large simulation box is required. For economy, we resorted to a multiscale approach using a combination of continuum and atomistic simulation. In continuum simulations, the ionic transport through the Si_3N_4 membrane is described by the coupled PNP (9) and the Stokes equations (10), which are solved in a self-consistent manner to obtain a converged solution for the ion transport (11). Specifically, the PNP and the Stokes equations are solved iteratively until a self-consistent solution for the concentration of the ions; electrical potential and the bulk velocity are obtained. The net current density through the pore is then given by $J = F \sum_{i=1}^{N} z_i \Gamma_i$, where N is the total number of ionic species, z_i is the valence of the ith species, and Γ_i is the axial component (*z*-direction in the present work) of the flux of the ith species. The axial flux of the ith species is given by the expression (25)

$$\Gamma_i = -D_i \frac{\partial c_i}{\partial z} - \mu_i z_i c_i \frac{\partial \Phi}{\partial z} + c_i u,$$

where D_i is the diffusion coefficient, μ_i is the ionic mobility (extracted from MD simulations), c_i is the concentration of the ith species, u is the axial velocity of the bulk flow, and Φ is the electrical potential. This approach has been used by several research groups to study the ionic transport in biological ion channels (34, 35). MD simulations provide the average ionic mobility only at particular locations in the pore that correspond to the center of each bin. A linear interpolation between the points is then used to obtain mobility variation in the entire pore. The diffusivity is assumed to be proportional to the ionic mobility, i.e., $D_i = D_i^{bulk} \mu_i / \mu_i^{bulk}$.

As shown in Fig. 4*a*, a substantial amount of counterions (K^+) are adsorbed on pore surface because of the strong local electric field created by the partial charges. The absorbed counterions have extremely low mobility; their contribution to the net current through the nanopore is therefore negligible. To account for the absorbed ions in the continuum simulation, the effective surface

of the pore is shifted toward the center of the pore by 0.19 nm so that only the region where the ions are mobile is considered. The corresponding surface charge density of the reduced pore is the sum of the original surface charge density of the pore, $\rho_0 = -0.02$ C/m², and the adsorbed surface charge density (ρ_{ads}), i.e., $\rho = \rho_0 + \rho_{ads}$. The (Stern layer) adsorption of the counterions is described by the Langmuir isotherm (36)

$$\rho_{ads} = \frac{A c_{counterions}^{W}}{1 + B c_{counterions}^{W}},$$

where $c_{counterions}^{W}$ is the concentration of the mobile counterions at the solid–liquid interface. The parameters A and B are extracted by computing ρ_{ads} in MD simulation at two different bath concentrations. By using the combined continuum/MD approach, the ionic conductivity of the Si_3N_4 nanopore connected with a KCl bath of concentrations 1 M, 100 mM, and 10 mM was examined.

Fig. 5 *a* and *b* shows a comparison of the ionic conductance and conductivity obtained from multiscale simulation and experiments at 1.0 M bath concentration. Notice that the pore conductivity is always less than the bulk conductivity. Although the multiscale simulation underestimates the conductivity for the smallest pore, and overestimates it for the larger pores, it agrees with the experimental estimates within the error. The ionic conductance and conductivity for bath concentrations of 100 and 10 mM are shown in Fig. 5 *c–f*. In Fig. 5*d*, the pore conductivity at 100 mM first decreases with shrinking pore radius until $R_p \approx 1$ nm and then slowly increases as the pore is becoming smaller. At 10 mM, the pore conductivity always increases with decreasing pore size, where the increase is more significant for the smaller pores ($R_p = 0.75$ and 0.5 nm) compared with the larger pores ($R_p > 1$ nm), as shown in Fig. 5*f*. Notice that the conductivity of the smallest pore ($R_p = 0.5$ nm) is about the same for all of the bath concentrations.

To understand the scaling behavior of the conductivity, changes in the average concentration and ionic mobility have to be taken into account. The ionic mobility typically decreases with decreasing pore radius due to increased confinement and surface field effects. For high bath concentrations (1 M), the variation of average concentration with pore size is small, and so

the conductivity scales with ionic mobility (Fig. 5*b*). However, for a dilute bath concentration (10 mM), the average concentration increases significantly with decreasing pore size as a large number of ions (that are dictated by the surface charge) are confined to a smaller volume. Consequently, the increase in average concentration outweighs the decrease in the mobility; therefore, conductivity increases with decreasing pore radius (Fig. 5*f*). For intermediate bath concentrations (100 mM), the decrease of ionic mobility and the increase of average concentration with decreasing pore size both play an important role in determining the pore conductivity.

In summary, we have inferred the conductivity and ionic mobility through nanopores from measurements of the ionic conductance as a function of time and bath concentration. The pore conductivity is found to be much larger than the bulk value for dilute bath concentrations (10 mM), where the Debye length is larger than the pore radius; conversely, it is comparable to or less than the bulk for high bath concentrations (1 M). We interpret these observations by using multiscale simulations of the ion transport through the pores and find that the measurements are consistent with the presence of fixed negative charge in the pore wall and a reduction of the ion mobility due to the fixed charge and the ion proximity to the pore wall.

1. Finkelstein, A. (1985) *Ann. N.Y. Acad. Sci.* **456,** 26–32.
2. Weinreb, G. E. & Maqura, I. S. (1998) *Neurophysiology* **30,** 325–327.
3. Lee S. H. & Rasaiah, J. C. (1996) *J. Phys. Chem.* **100,** 1420–1425.
4. Koneshan, S., Rasaiah, J. C., Lynden-Bell, R. M. & Lee, S. H. (1998) *J. Phys. Chem.* **102,** 4193–4204.
5. Lynden-Bell, R. M. & Rasaiah, J. C. (1996) *J. Chem. Phys.* **105,** 9266–9280.
6. Siwy, Z. & Fuliński, A. (2002) *Phys. Rev. Lett.* **89,** 198103.
7. Schmid, G. & Schwarz, H. (1998) *J. Membr. Sci.* **150,** 171–187.
8. Stein, D., Kruithof, M. & Dekker, C. (2004) *Phys. Rev. Lett.* **93,** 035901.
9. Oldham, K. B. & Myland, J. C. (1994) *Fundamentals of Electrochemical Science* (Academic, San Diego).
10. White, F. M. (1992) *Fluid Mechanics* (McGraw–Hill, New York).
11. Chatterjee, A., Cannon, D., Gatimu, E., Sweedler, J., Aluru, N. R. & Bohn, P. W. (2005) *J. Nanopart. Res.*, in press.
12. Li, J., Stein, D., McMullan, C., Branton, D., Aziz, M. J. & Golovchenko, J. A. (2001) *Nature* **412,** 166–169.
13. Martin, C. R., Nishizawa, M., Jirage, K., Kang, M. & Lee S. B. (2001) *Adv. Mater.* **13,** 1351–1362.
14. Storm, A. J., Chen, J. H., Ling, X. S., Zandbergen, H. W. & Dekker. C. (2003) *Nat. Mater.* **2,** 537–540.
15. Chang, H., Kosari, F., Andreadakis, G., Alam, M. A., Vasmatzis, G. & Bashir, R. (2004) *Nano Lett.* **4,** 1551–1556.
16. Okamura, Y., Gotoh, K., Kosaka, M. & Tagawa, M. (1998) *J. Adhes. Sci. Technol.* **12,** 639–654.
17. Liu, A. J., Durian, D. J., Herbolzheimer, E. & Safran, S. A. (1990) *Phys. Rev. Lett.* **65,** 1897–1900.
18. Restagno, F., Bocquet, L. & Biben, T. (2000) *Phys. Rev. Lett.* **84,** 2433–2436.
19. Restagno, F., Bocquet, L., Biben, T. & Charlaix, E. (2000) *J. Phys. Condensed Matter* **12,** A419–A424.
20. Restagno, F., Bocquet, L., Crassous, J. & Charlaix, E. (2002) *Colloid Surf. A* **206,** 69–77.
21. Jiang, J. Z., Stahl, K., Berg, B. W., Frost, D. J., Zhou, T. J. & Shi, P. X. (2000) *Europhys. Lett.* **51,** 62.
22. Wendel, J. A. & Goddard, W. A. (1992) *J. Chem. Phys.* **97,** 5048–5062.
23. Aksimentiev, A., Heng, J. B., Timp, G. & Schulten, K. (2004) *Biophys. J.* **87,** 2086–2097.
24. Cerovic, L. S., Milonjic, S. K., Bahloul-Hourlier, D. & Doucey, B. (2002) *Colloid Surf. A* **197,** 147–156.
25. Sonnefeld, J. (1996) *Colloid Surf. A* **108,** 27–31.
26. Berendsen, H. J. C., Grigera, J. R. & Straatsma, T. P. (1987) *J. Phys. Chem.*, **91,** 6269–6271.
27. van der Spoel, D., van Buuren, A. R., Apol, E., Meulenhoff, P. J., Tieleman, D. P., Sijbers, A. L. T. M., Hess, B., Feenstra, K. A., Lindahl, E., van Drunen, R. & Berendsen, H. J. C. (2001) GROMACS *User Manual* (University of Groningen, Groningen, The Netherlands), Version 3.0.
28. Lindahl, E., Hess, B. & van der Spoel, D. (2001) *J. Mol. Modell.* **7,** 306–317.
29. Darden, T., York, D. & Pedersen, L. (1993) *J. Chem. Phys.* **98,** 10089–10092.
30. Crozier, P. S., Henderson, D., Rowley, R. L. & Busath, D. D. (2001) *Biophys. J.* **81,** 3077–3089.
31. Qiao, R. & Aluru, N. R. (2003) *J. Chem. Phys.* **118,** 4692–4701.
32. Israelachvili, J. (1992) *Intermolecular and Surface Forces* (Academic, New York).
33. Zhou, J. D., Cui, S. T. & Cochran, H. D. (2003) *Mol. Phys.* **101,** 1089–1094.
34. Adcock, C., Smith, G. R. & Sansom, M. S. P. (2000) *Euro. Biophys. J.* **29,** 29–37.
35. Berneche, S. & Roux, B. (2003) *Proc. Natl. Acad. Sci. USA,* **100,** 8644–8648.
36. Paces, M., Kosek, J., Marek, M., Tallarek, U. & Seidel-Morgenstern, A. (2003) *Electrophoresis* **24,** 380–389.